

Doppler velocity detection limitations in spectrometer-based versus swept-source optical coherence tomography

Hansford C. Hendargo,^{1,*} Ryan P. McNabb,¹ Al-Hafeez Dhalla,¹ Neal Shepherd,² and Joseph A. Izatt¹

¹Department of Biomedical Engineering, Duke University, 136 Hudson Hall, Box 90281, Durham, NC 27708, USA

²Jean and George Brumley Jr. Neonatal-Perinatal Research Institute,

Department of Pediatrics/Division of Neonatology—Duke University Medical Center, Box 103105, Durham, NC 27710, USA

*Hansford.hendargo@duke.edu

Abstract: Recent advances in Doppler techniques have enabled high sensitivity imaging of biological flow to measure blood velocities and vascular perfusion. Here we compare spectrometer-based and wavelength-swept Doppler OCT implementations theoretically and experimentally, characterizing the lower and upper observable velocity limits in each configuration. We specifically characterize the washout limit for Doppler OCT, the velocity at which signal degradation results in loss of flow information, which is valid for both quantitative and qualitative flow imaging techniques. We also clearly differentiate the washout effect from the separate phenomenon of phase wrapping. We demonstrate that the maximum detectable Doppler velocity is determined by the fringe washout limit and not phase wrapping. Both theory and experimental results from phantom flow data and retinal blood flow data demonstrate the superiority of the swept-source technique for imaging vessels with high flow rates.

© 2011 Optical Society of America

OCIS codes: (170.2655) Functional monitoring and imaging; (170.3340) Laser Doppler velocimetry; (170.4500) Optical coherence tomography

References and links

1. Z. Chen, T. E. Milner, D. Dave, and J. S. Nelson, "Optical Doppler tomographic imaging of fluid flow velocity in highly scattering media," *Opt. Lett.* **22**(1), 64–66 (1997).
2. J. A. Izatt, M. D. Kulkarni, S. Yazdanfar, J. K. Barton, and A. J. Welch, "In vivo bidirectional color Doppler flow imaging of picoliter blood volumes using optical coherence tomography," *Opt. Lett.* **22**(18), 1439–1441 (1997).
3. R. Leitgeb, C. K. Hitzenberger, and A. F. Fercher, "Performance of fourier domain vs. time domain optical coherence tomography," *Opt. Express* **11**(8), 889–894 (2003).
4. M. A. Choma, M. V. Sarunic, C. Yang, and J. A. Izatt, "Sensitivity advantage of swept source and Fourier domain optical coherence tomography," *Opt. Express* **11**(18), 2183–2189 (2003).
5. J. F. de Boer, B. Cense, B. H. Park, M. C. Pierce, G. J. Tearney, and B. E. Bouma, "Improved signal-to-noise ratio in spectral-domain compared with time-domain optical coherence tomography," *Opt. Lett.* **28**(21), 2067–2069 (2003).
6. R. K. Wang, S. L. Jacques, Z. Ma, S. Hurst, S. R. Hanson, and A. Gruber, "Three dimensional optical angiography," *Opt. Express* **15**(7), 4083–4097 (2007).
7. Y. K. Tao, A. M. Davis, and J. A. Izatt, "Single-pass volumetric bidirectional blood flow imaging spectral domain optical coherence tomography using a modified Hilbert transform," *Opt. Express* **16**(16), 12350–12361 (2008).
8. M. Szkulmowski, A. Szklomska, T. Bajraszewski, A. Kowalczyk, and M. Wojtkowski, "Flow velocity estimation using joint Spectral and Time domain Optical Coherence Tomography," *Opt. Express* **16**(9), 6008–6025 (2008).
9. Y. K. Tao, K. M. Kennedy, and J. A. Izatt, "Velocity-resolved 3D retinal microvessel imaging using single-pass flow imaging spectral domain optical coherence tomography," *Opt. Express* **17**(5), 4177–4188 (2009).
10. R. K. Wang and L. An, "Doppler optical micro-angiography for volumetric imaging of vascular perfusion in vivo," *Opt. Express* **17**(11), 8926–8940 (2009).

11. I. Grulkowski, I. Gorczynska, M. Szkulmowski, D. Szlag, A. Szkulmowska, R. A. Leitgeb, A. Kowalczyk, and M. Wojtkowski, "Scanning protocols dedicated to smart velocity ranging in spectral OCT," *Opt. Express* **17**(26), 23736–23754 (2009).
12. Y. Yasuno, S. Makita, T. Endo, G. Aoki, M. Itoh, and T. Yatagai, "Simultaneous B-M-mode scanning method for real-time full-range Fourier domain optical coherence tomography," *Appl. Opt.* **45**(8), 1861–1865 (2006).
13. A. H. Bachmann, M. L. Villiger, C. Blatter, T. Lasser, and R. A. Leitgeb, "Resonant Doppler flow imaging and optical vivisection of retinal blood vessels," *Opt. Express* **15**(2), 408–422 (2007).
14. F. Jaillon, S. Makita, M. Yabasaki, and Y. Yasuno, "Parabolic BM-scan technique for full range Doppler spectral domain optical coherence tomography," *Opt. Express* **18**(2), 1358–1372 (2010).
15. A. Mariampillai, B. A. Standish, E. H. Moriyama, M. Khurana, N. R. Munce, M. K. K. Leung, J. Jiang, A. Cable, B. C. Wilson, I. A. Vitkin, and V. X. D. Yang, "Speckle variance detection of microvasculature using swept-source optical coherence tomography," *Opt. Lett.* **33**(13), 1530–1532 (2008).
16. J. Fingler, D. Schwartz, C. Yang, and S. E. Fraser, "Mobility and transverse flow visualization using phase variance contrast with spectral domain optical coherence tomography," *Opt. Express* **15**(20), 12636–12653 (2007).
17. J. Fingler, R. J. Zawadzki, J. S. Werner, D. Schwartz, and S. E. Fraser, "Volumetric microvascular imaging of human retina using optical coherence tomography with a novel motion contrast technique," *Opt. Express* **17**(24), 22190–22200 (2009).
18. L. Yu and Z. Chen, "Doppler variance imaging for three-dimensional retina and choroid angiography," *J. Biomed. Opt.* **15**(1), 016029 (2010).
19. S. Zotter, M. Pircher, T. Torzicky, M. Bonesi, E. Götzinger, R. A. Leitgeb, and C. K. Hitzenberger, "Visualization of microvasculature by dual-beam phase-resolved Doppler optical coherence tomography," *Opt. Express* **19**(2), 1217–1227 (2011).
20. S. Makita, F. Jaillon, M. Yamanari, M. Miura, and Y. Yasuno, "Comprehensive in vivo micro-vascular imaging of the human eye by dual-beam-scan Doppler optical coherence angiography," *Opt. Express* **19**(2), 1271–1283 (2011).
21. M. A. Choma, A. K. Ellerbee, S. Yazdanfar, and J. A. Izatt, "Doppler flow imaging of cytoplasmic streaming using spectral domain phase microscopy," *J. Biomed. Opt.* **11**(2), 024014 (2006).
22. Y. Wang, B. A. Bower, J. A. Izatt, O. Tan, and D. Huang, "In vivo total retinal blood flow measurement by Fourier domain Doppler optical coherence tomography," *J. Biomed. Opt.* **12**(4), 041215 (2007).
23. Y. Wang, B. A. Bower, J. A. Izatt, O. Tan, and D. Huang, "Retinal blood flow measurement by circumapillary Fourier domain Doppler optical coherence tomography," *J. Biomed. Opt.* **13**(6), 064003 (2008).
24. B. Baumann, B. Potsaid, M. F. Kraus, J. J. Liu, D. Huang, J. Horngger, A. E. Cable, J. S. Duker, and J. G. Fujimoto, "Total retinal blood flow measurement with ultrahigh speed swept source/Fourier domain OCT," *Biomed. Opt. Express* **2**(6), 1539–1552 (2011).
25. Y. Wang, A. Fawzi, O. Tan, J. Gil-Flamer, and D. Huang, "Retinal blood flow detection in diabetic patients by Doppler Fourier domain optical coherence tomography," *Opt. Express* **17**(5), 4061–4073 (2009).
26. C. E. Riva, J. E. Grunwald, S. H. Sinclair, and B. L. Petrig, "Blood velocity and volumetric flow rate in human retinal vessels," *Invest. Ophthalmol. Vis. Sci.* **26**(8), 1124–1132 (1985).
27. J. Walther, G. Mueller, H. Morawietz, and E. Koch, "Signal power decrease due to fringe washout as an extension of the limited Doppler flow measurement range in spectral domain optical coherence tomography," *J. Biomed. Opt.* **15**(4), 041511 (2010).
28. S. H. Yun, G. J. Tearney, J. de Boer, and B. E. Bouma, "Motion artifacts in optical coherence tomography with frequency-domain ranging," *Opt. Express* **12**(13), 2977–2998 (2004).
29. J. A. Izatt and M. A. Choma, "Theory of optical coherence tomography," in *Optical Coherence Tomography: Technology and Applications*, W. Drexler, and J. G. Fujimoto, eds. (Springer, 2008), pp. 47–72.
30. M. Pircher, B. Baumann, E. Götzinger, H. Sattmann, and C. K. Hitzenberger, "Phase contrast coherence microscopy based on transverse scanning," *Opt. Lett.* **34**(12), 1750–1752 (2009).
31. B. J. Vakoc, G. J. Tearney, and B. E. Bouma, "Statistical properties of phase-decorrelation in phase-resolved Doppler optical coherence tomography," *IEEE Trans. Med. Imaging* **28**(6), 814–821 (2009).
32. S. Yazdanfar, C. Yang, M. V. Sarunic, and J. A. Izatt, "Frequency estimation precision in Doppler optical coherence tomography using the Cramer-Rao lower bound," *Opt. Express* **13**(2), 410–416 (2005).
33. B. H. Park, M. C. Pierce, B. Cense, S.-H. Yun, M. Mujat, G. J. Tearney, B. E. Bouma, and J. de Boer, "Real-time fiber-based multi-functional spectral-domain optical coherence tomography at 1.3 microm," *Opt. Express* **13**(11), 3931–3944 (2005).
34. B. J. Vakoc, S. H. Yun, J. de Boer, G. J. Tearney, and B. E. Bouma, "Phase-resolved optical frequency domain imaging," *Opt. Express* **13**(14), 5483–5493 (2005).
35. M. A. Choma, A. K. Ellerbee, C. Yang, T. L. Creazzo, and J. A. Izatt, "Spectral-domain phase microscopy," *Opt. Lett.* **30**(10), 1162–1164 (2005).
36. B. A. Bower, M. Zhao, R. J. Zawadzki, and J. A. Izatt, "Real-time spectral domain Doppler optical coherence tomography and investigation of human retinal vessel autoregulation," *J. Biomed. Opt.* **12**(4), 041214 (2007).
37. B. R. White, M. C. Pierce, N. Nassif, B. Cense, B. H. Park, G. J. Tearney, B. E. Bouma, T. C. Chen, and J. de Boer, "In vivo dynamic human retinal blood flow imaging using ultra-high-speed spectral domain optical coherence tomography," *Opt. Express* **11**(25), 3490–3497 (2003).
38. R. A. Leitgeb, L. Schmetterer, W. Drexler, A. F. Fercher, R. J. Zawadzki, and T. Bajraszewski, "Real-time assessment of retinal blood flow with ultrafast acquisition by color Doppler Fourier domain optical coherence tomography," *Opt. Express* **11**(23), 3116–3121 (2003).

39. C. Joo, T. Akkin, B. Cense, B. H. Park, and J. F. de Boer, "Spectral-domain optical coherence phase microscopy for quantitative phase-contrast imaging," *Opt. Lett.* **30**(16), 2131–2133 (2005).
40. H. C. Hendargo, M. Zhao, N. Shepherd, and J. A. Izatt, "Synthetic wavelength based phase unwrapping in spectral domain optical coherence tomography," *Opt. Express* **17**(7), 5039–5051 (2009).
41. S. H. Yun, G. J. Tearney, J. de Boer, and B. E. Bouma, "Pulsed-source and swept-source spectral-domain optical coherence tomography with reduced motion artifacts," *Opt. Express* **12**(23), 5614–5624 (2004).
42. L. Wang, Y. Wang, S. Guo, J. Zhang, M. Bachman, G. P. Li, and Z. Chen, "Frequency domain phase-resolved optical Doppler and Doppler variance tomography," *Opt. Commun.* **242**(4-6), 345–350 (2004).
43. S. Makita, Y. Hong, M. Yamanari, T. Yatagai, and Y. Yasuno, "Optical coherence angiography," *Opt. Express* **14**(17), 7821–7840 (2006).
44. D. C. Ghiglia and M. D. Pritt, *Two-Dimensional Phase Unwrapping: Theory, Algorithms, and Software* (Wiley-Interscience, New York, 1998).
45. S. T. Flock, S. L. Jacques, B. C. Wilson, W. M. Star, and M. J. van Gemert, "Optical properties of Intralipid: a phantom medium for light propagation studies," *Lasers Surg. Med.* **12**(5), 510–519 (1992).
46. J. A. Curcio and C. C. Petty, "The Near Infrared Absorption Spectrum of Liquid Water," *J. Opt. Soc. Am.* **41**(5), 302–304 (1951).
47. A. Roggan, M. Friebel, K. Dörschel, A. Hahn, and G. Müller, "Optical Properties of Circulating Human Blood in the Wavelength Range 400–2500 nm," *J. Biomed. Opt.* **4**(1), 36–46 (1999).
48. P. H. M. Bovendeerd, A. A. Steenhoven, F. N. Vosse, and G. Vossers, "Steady entry flow in a curved pipe," *J. Fluid Mech.* **177**(-1), 233–246 (1987).
49. G. T. Feke, H. Tagawa, D. M. Deupree, D. G. Goger, J. Sebag, and J. J. Weiter, "Blood flow in the normal human retina," *Invest. Ophthalmol. Vis. Sci.* **30**(1), 58–65 (1989).

1. Introduction

Doppler optical coherence tomography [1,2] has been demonstrated to have important potential uses in functional imaging and diagnostics, particularly in the field of ophthalmology. Spectrometer-based and wavelength-swept Fourier domain OCT have undergone rapid development due to their demonstrated advantages in imaging speed and sensitivity over time domain systems [3–5]. Recent advances in Doppler and variance techniques have enabled high sensitivity for imaging regions of biological flow to measure blood velocities and vascular perfusion in microcapillary structures. These modalities use various techniques involving either dense sampling protocols [6–10], customized scanning procedures [11], phase modulation schemes [12–14], or variance and power Doppler methods [15–18] to acquire flow information. Recently, dual-beam techniques have also increased the dynamic range of detectable velocities [19,20]. The methods can further be categorized by their capability for quantitative velocity measurement, or else as a qualitative method for flow visualization. For velocity resolved measurements, the phase sensitivity of the OCT system governs the lowest observable velocity of a moving scatterer [21]. For the non-velocity resolved methods, speckle decorrelation produced by a moving sample causes variations in either the intensity or phase over time. In these cases, even Brownian motion of a fluid is sufficient to cause distinguishable changes from static structure [15,16].

Total retinal blood flow studies using Doppler volumes or circumpapillary scans have demonstrated a potentially important clinical application for Doppler imaging by providing a functional biomarker for disease diagnosis [22–24]. Differences in total retinal flow between normal and diabetic patients have also been demonstrated [25]. Because total retinal flow studies require imaging blood flow about the optic nerve head region, high flow rates are encountered [26] which pose a different set of imaging considerations compared to microvasculature flow. Problems hindering functional imaging in clinical systems include phase wrapping and interferometric fringe washout effects that occur in large blood vessels with fast flow rates. These problems prevent accurate assessment of the detected Doppler signal, creating ambiguities in the measurements in the case of phase wrapping and loss of flow information in the case of fringe washout. Though these artifacts are correlated with the speed of moving scatterers [27], precise detection and measurement are difficult in biological samples due to the loss of SNR that occurs as a result of the motion of sample scatterers. Swept-source systems have been shown to be more robust against this effect compared to spectrometer-based detection schemes [28].

The commercial availability of wavelength-swept sources has made them an increasingly attractive alternative to spectrometer-based systems. Comparative analysis of the potential

benefits and limitations for the various OCT configurations would be useful for matching technology capabilities to specific clinical problems. There has also been some ambiguity in the description of the limitations characterizing the upper velocity limit for Doppler systems. Typically, the maximum velocity is characterized as the speed at which a π phase shift is induced in the Doppler signal. However, it is possible to detect scatterers moving at even higher velocities, though the signal then suffers from phase wrapping artifacts. Flow information may still be recovered from such situations with sufficiently high image SNR and appropriate phase unwrapping methods. Thus, the maximum detectable velocity may be higher than the phase wrapping limit.

Here we present theoretical analysis and experimental results comparing the lower and upper observable velocity limits in spectrometer-based and swept-source Doppler OCT. We also define the fringe washout limit, the velocity of moving scatterers above which information loss occurs. To our knowledge, the artifacts of phase wrapping and fringe washout have not been clearly distinguished in past literature. Thus, we seek to clarify the causes and definitions of each of these phenomena that occur when imaging high speed flow. We also characterize the Doppler dynamic range of measurable flow velocities for a given OCT system.

2. Theory of Doppler velocity limitations

The interferometric expression for the detected signal in OCT, $i(k)$, for a single moving scatterer [29] can be written as

$$i(k) = \rho S(k) \left(R_r + R_s + \sqrt{R_r R_s} \operatorname{Re}\{\exp[-i2nk(\Delta z + v_z t)]\} \right). \quad (1)$$

Here, ρ is the detector responsivity, $S(k)$ is the source power spectral density, R_r and R_s are the reflectivities of the reference mirror and sample scatterer, n is the index of refraction of the sample, k is the wavenumber, Δz is the optical path length difference between the reference mirror and sample reflector, v_z is the axial velocity of the sample scatterer, and t is the time variable. The $\operatorname{Re}\{\}$ operator computes the real components of the complex expression corresponding to the detectable portion of the interferogram. The argument of the exponential yields the interferometric frequency corresponding to the path length difference between the sample arm reflector position and the reference arm mirror position. It can be seen that a non-zero velocity of the sample reflector results in an additional phase shift in the interferogram. Performing a Fourier transformation along k of the real signal detected yields a Hermitian symmetric expression

$$I(z) = \rho \gamma(z) \left(R_r + R_s \right) + \rho \sqrt{R_r R_s} \left\{ \gamma(z - \Delta z) \exp[j2nk_o v_z t] + \gamma(z + \Delta z) \exp[-j2nk_o v_z t] \right\}, \quad (2)$$

where $\gamma(z)$ is the autocorrelation function of $S(k)$ and k_o is the center wavenumber of the source. The phase of the reflector for one side of the complex conjugate term is given by

$$\phi = 2nk_o v_z t = \frac{4\pi n \delta z}{\lambda_o}, \quad (3)$$

with $\delta z = v_z t$ being the axial displacement caused by motion, and λ_o as the center wavelength of the source. The phase differences, $\Delta\phi$, between sequential A-scans at a given location allow for the detection of a Doppler shift frequency. This axial phase shift can be related to the velocity of the moving scatterer if the incident angle of the imaging beam to the direction of motion, θ_D , is known [21]:

$$v = \frac{\lambda_o \Delta\phi}{4\pi n T \cos \theta_D}, \quad (4)$$

in which T is the inverse A-scan line rate, or the time between acquisitions of sequential A-scans used for Doppler processing. T is determined by the detector line integration plus readout time for spectrometer systems or by the time for both a forward and reverse wavelength sweep in swept-source systems.

2.1. Minimum detectable velocity

The theoretical flow sensitivity (minimum observable velocity) for conventional Doppler OCT processing is limited by the phase sensitivity, $\delta\phi$, of the system. Factors influencing phase sensitivity include mechanical stability [30], decorrelation [31], image SNR [32,33], and timing induced errors for the case of swept-source systems [34]. An expression characterizing the lower velocity limit is given by [21]

$$v_{\min} = \frac{\lambda_o \delta\phi}{4\pi n T \cos \theta_D} = \frac{\lambda_o}{2\pi^2 n T \cos \theta_D} \frac{1}{\sqrt{SNR}}. \quad (5)$$

On the right, Eq. (5) is expanded to include an expression for phase sensitivity at the shot noise-limited SNR of the imaging system [35]. At the shot-noise limit, v_{\min} is the same for spectrometer-based and swept-source systems and is determined by the performance characteristics of the optical and detection setup.

2.2. Phase wrapping threshold velocity

Because the detected phase is limited to the interval $[-\pi, \pi]$, the upper unambiguous velocity limit corresponds to a phase shift of π radians between sequential A-scan acquisitions. Should the velocity of the sample induce a phase shift greater than π , the measured phase will wrap to the opposite end of the detectable phase range, yielding an ambiguous result. Thus, the expression governing this phase wrapping artifact is given by [36–38]

$$v_{\text{wrap}} = \frac{\lambda_o}{4nT \cos \theta_D}. \quad (6)$$

The variable definitions in this expression are the same as for Eq. (5), thus the phase wrapping threshold velocity is also expected to be the same for spectrometer-based and swept-source systems. It should be emphasized that T is the time between A-scan acquisitions used to calculate the Doppler phase shift. Although various approaches have been explored for phase unwrapping in Doppler and phase-microscope versions of OCT [39,40], this remains a difficult problem in biological imaging and is a serious limitation for clinical applications of Doppler OCT such as total retinal blood flow estimation [22].

2.3. Fringe washout threshold velocity

The integration time for an A-scan is given by DT , where D is the detector duty cycle. The duty cycle is the fraction of the time over which the detector is actively integrating the optical signal in spectrometer-based systems or the fractional time of the usable wavelength sweep in swept-source systems (typically the forward sweep). It has been shown that by integrating the signal in Eq. (1) for spectrometer-based OCT over the period of DT , axial motion of a sample may cause significant SNR degradation according to the resulting sinc factor as shown in Eq. (8) [28]:

$$i(k) = S(k) \int_0^{DT} R_r + R_s + \sqrt{R_r R_s} \operatorname{Re}\{\exp[-i2nk(\Delta z + v_z t)]\} dt, \quad (7)$$

$$i(k) = S(k) \left(R_r + R_s + \sqrt{R_r R_s} \operatorname{Re}\{\exp[-i2nk\Delta z]\} \frac{\sin(2nkv_z DT)}{2nkv_z DT} \right) DT. \quad (8)$$

The sinc factor gives rise to an artifact known as fringe washout, a condition in which phase shifts caused by sample motion result in signal loss. SNR degradation occurs because the amplitude of the interferometric fringe pattern decreases due to averaging of the signal over the integration time of each of the detector spectral channels. While it has been shown that swept-source systems are more robust against fringe washout effects as compared to spectrometer-based systems [28,34], the washout effect will still be present in swept-source configurations at high flow velocities.

For a swept-source system with M spectral samples per A-scan, the integration time per spectral channel may be defined as $\tau = DT/M$ [41]. Modifying the expression in Eq. (7) to integrate over τ yields

$$i(k) = S(k) \int_0^\tau R_r + R_s + \sqrt{R_r R_s} \operatorname{Re}\{\exp[-i2nk(\Delta z + v_z t)]\} dt, \quad (9)$$

$$i(k) = S(k) \left(R_r + R_s + \sqrt{R_r R_s} \operatorname{Re}\{\exp[-i2nk\Delta z]\} \frac{\sin(2nkv_z \tau)}{2nkv_z \tau} \right) \tau. \quad (10)$$

For the case of spectrometer-based systems, each spectral channel is summed over the duty cycle of the line acquisition time of the detector camera. Because all spectral channels are acquired in parallel, this results in $\tau = DT$ which reduces Eq. (10) to Eq. (8). For swept-source systems, however, each spectral channel is acquired in series, effectively leading to a much higher spectral sampling rate according to the number of samples per sweep. A higher spectral sampling rate can also be achieved in spectrometer-based systems using pulsed illumination of the spectrometer to ensure integration over only a small portion of the spectral interference fringe [41]. It can be seen that swept-source systems will still suffer the same SNR degradation at high velocities. However, this limit is M times greater than in spectrometer-based systems if the duty cycles of the wavelength sweep and the spectrometer line acquisition are equal. Thus for Doppler imaging, one would expect that faster flow velocities may be detected in swept-source systems without loss of signal. It should be noted that phase wrapping occurs due to phase shifts between sequential A-scans used to calculate the Doppler shift. Fringe washout differs in that it is caused by phase shifts over the duration of a single A-scan acquisition and is directly related to the sinc factor in Eq. (10).

To our knowledge, a simple expression comparable to those above for v_{min} and v_{wrap} for the effect of fringe washout (which also clearly differentiates this effect from phase wrapping) has not yet been published. Physically, fringe washout occurs when the sample motion is sufficient to cause approximately a π phase shift in the spectral interferogram during the acquisition of each spectral resolution element. This also corresponds to the first zero of the sinc falloff factor previously described in Eq. (10). The velocity at which this occurs is

$$v_{wash} = \frac{\lambda_o}{4n\tau \cos \theta_D}. \quad (11)$$

which parallels Eq. (6) with the exception that v_{wash} is determined by the spectral channel sampling time set by τ rather than the time between A-scan acquisitions.

If the spectral sampling rate, τ^{-1} , is below the Nyquist sampling limit required for reconstruction of the interference fringes, washout occurs. For spectrometer-based systems, v_{wash} is determined by the active integration time over the detector duty cycle, $\tau = DT$, and thus exceeds v_{wrap} only by a factor of $1/D$. However, for swept-source systems, v_{wash} increases linearly with M , leading to an increase in velocity of M/D over v_{wrap} . In swept-source systems one may observe many phase wraps before fringe washout causes significant SNR loss. Since $\tau \ll DT$ for swept-source systems, these systems have a much higher spectral sampling rate, thus leading to an important advantage in maximum observable velocity compared to spectrometer-based Doppler OCT systems.

Figure 1 illustrates the comparative advantage of swept-source Doppler over spectrometer-based Doppler as theoretically calculated from Eqs. (5), (6), and (11) for systems with a 20 kHz A-scan rate, unity duty cycle, 830 nm source, 1024 detector channels, and a reflector with a given SNR of 40 dB. In this simulation, the swept-source washout limit is three orders of magnitude higher than the spectrometer-based system due to the rapid integration time per wavelength channel.

A useful characterization of Doppler OCT performance is the Doppler dynamic range, or the ratio of the maximum detectable velocity to the minimum observable velocity,

$$\text{Doppler dynamic range} = \frac{v_{\text{wash}}}{v_{\text{min}}} = \frac{\pi^2 \sqrt{\text{SNR}} T}{2 \tau}. \quad (12)$$

It can be seen that for Doppler measurements in which sequential A-scans are used to calculate Doppler frequency shifts, swept-source systems have a velocity dynamic range gain of M over spectrometer-based systems. Thus, swept-source Doppler has a significant advantage for imaging a wide range of flow rates without suffering the signal degradation that occurs when imaging high velocity scatterers with spectrometer-based systems. Table 1 summarizes the derived expressions for Doppler velocity detection limits in OCT including expressions for characterizing the Doppler dynamic range for spectrometer-based and swept-source OCT. Note the differences for v_{wash} and the Doppler dynamic range expressions between the two OCT configurations.

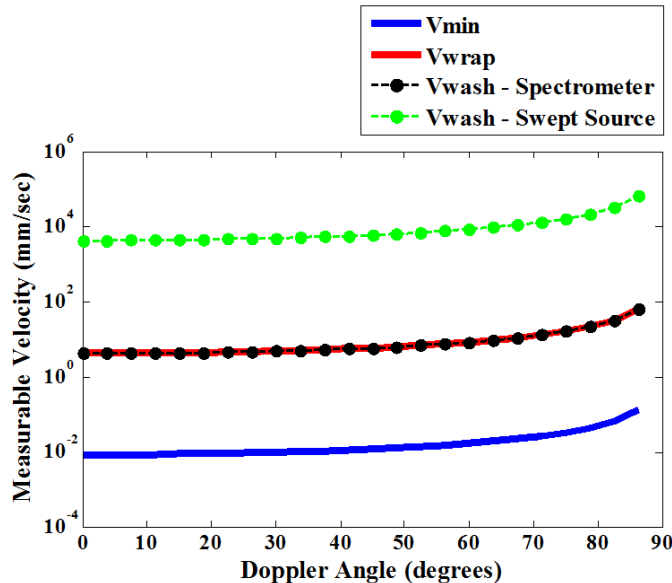


Fig. 1. Theoretical predictions for velocity limitations of swept-source and spectrometer-based Doppler OCT systems. The minimum velocity and wrapping velocity are the same for both systems. The spectrometer-based washout velocity equals the wrapping velocity, but the washout limit is several orders of magnitude greater for the swept-source system.

Table 1. Summary of Doppler OCT velocity detection limits

Velocity Limit	Spectrometer-Based OCT Expression	Swept-Source OCT Expression	Determining Factor
Minimum velocity (V_{\min})	$\frac{\lambda_o}{2\pi^2 nT \cos \theta_d} \frac{1}{\sqrt{SNR}}$	$\frac{\lambda_o}{2\pi^2 nT \cos \theta_d} \frac{1}{\sqrt{SNR}}$	Image SNR
Wrapping velocity (V_{wrap})	$\frac{\lambda_o}{4nT \cos \theta_d}$	$\frac{\lambda_o}{4nT \cos \theta_d}$	Time between A-scan acquisitions
Washout velocity (V_{wash})	$\frac{\lambda_o}{4nDT \cos \theta_d}$	$\frac{M \lambda_o}{4nDT \cos \theta_d}$	Time to acquire single spectral channel
Doppler dynamic range (V_{wash}/V_{\min})	$\frac{\pi^2 \sqrt{SNR}}{2D}$	$\frac{M \pi^2 \sqrt{SNR}}{2D}$	Image SNR and number of spectral channels

3. Methods

To experimentally demonstrate the Doppler advantage of swept-source over spectrometer-based systems, a flow phantom of 1% intralipid was imaged using the systems shown in Fig. 2. The spectrometer-based system consisted of a broadband source (SuperLum, $\lambda_o = 830$ nm, $\Delta\lambda = 60$ nm) and custom spectrometer (Basler, 100 kHz line rate, 87% duty cycle, 2048 pixels). To measure the phase stability of the system, a glass coverslip was imaged with an SNR of 53 dB. Phase differences of the front coverslip surface over 1000 A-scans were acquired, and the phase stability was defined as the standard deviation of the phase differences [24,34], measured at 4 mrad. The swept-source system used a wavelength swept laser (Axsun, $\lambda_o = 1040$ nm, $\Delta\lambda = 100$ nm, 100 kHz, 50% duty cycle, 1376 samples/sweep) and a dual balanced photodiode detector (New Focus, 80 MHz bandwidth) with a 12 bit digitizer card (Alazar Tech, 500 MSamples/s). In order to compensate for the phase errors induced by fluctuations in the data acquisition trigger generated by the light source, an external fiber Bragg grating with a narrow linewidth (OE Land, $\lambda_o = 989$ nm, $\Delta\lambda = 0.042$ nm) was used to trigger the start of the acquisition for each wavelength sweep. The phase stability of the swept-source system was measured in the same manner as the spectrometer-based system. The signal from the coverslip surface was measured to be 64 dB and had a phase stability of 7 mrad.

Flow of various velocities was generated by a syringe pump (Harvard Apparatus). Because each system utilized different center wavelengths, a Doppler angle of $\theta_D = 73.7^\circ$ was used for the spectrometer-based system while an angle of $\theta_D = 69.4^\circ$ was used for the swept-source system to maintain similar Doppler frequency shifts for a given flow rate set by the pump. Data was acquired using 200 A-scans over 2 mm with x9 oversampling for both systems. The Doppler shift frequency was computed by taking the average phase of the complex difference between sequential A-scans at each lateral position as described in [42], and the velocity was computed according to Eq. (4). The Doppler angle was confirmed from a volume data set taken over the capillary tube structure. For comparative performance between the two systems, the measured velocity was normalized to the wrapping velocity as calculated from Eq. (6) for each system yielding

$$V' = \frac{v_{\text{measured}}}{v_{\text{wrap}}} \quad (13)$$

The peak SNR measured for each system was 95 dB. Thus, the calculated Doppler dynamic range for the spectrometer-based system was 55 dB and that of the swept-source system was 89 dB, showing that a significantly larger velocity range may be detected using the swept-source configuration.

All human data was obtained from a subject consented under an institutional review board approved protocol for imaging. To acquire retinal Doppler data, a commercial SDOCT system (Bioptrigen, Inc., $\lambda_0 = 840$ nm, $\Delta\lambda = 49$ nm, 20 kHz) was used. This system was chosen to demonstrate the problems faced in clinical systems with imaging areas of the retina with high blood flow rates. Though the acquisition rate was five times slower than the swept-source system, the images collected were similar to standard clinical quality. A Doppler volume consisting of 512x50 lines with x6 oversampling was acquired over the optic nerve region in 7.68 seconds. Data was interpolated to be linear in k prior to Fourier transformation. For Doppler data sets with oversampled A-scans, the magnitude data was averaged across the oversampled A-scans. Doppler phase processing was performed in the same manner as with the phantom data. Low signal regions were suppressed with an intensity threshold based on the magnitude data. Bulk motion was corrected using a histogram based method [43]. A 3x3 median filter was used to smooth the Doppler data. A color threshold to eliminate small Doppler signals caused by residual bulk motion artifacts was applied. Overlaid images of the magnitude and Doppler data were created for display.

The swept-source system in Fig. 2(B) was adapted for retinal imaging with 1.7 mW incident on the cornea. A Doppler volume consisting of 256x200 lines with x6 oversampling was acquired in 3.07 seconds. The swept-source system utilized a linear k-clock, thus avoiding the need for resampling. After Fourier transformation, the Doppler phase and magnitude data were processed the same way as detailed for the spectrometer-based data.

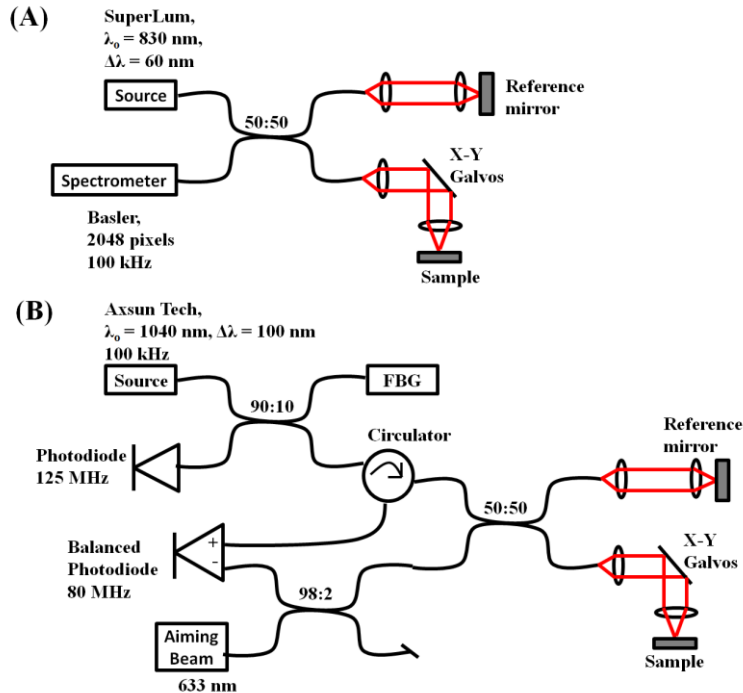


Fig. 2. Schematics of spectrometer-based and swept-source systems used in the comparative Doppler phantom experiments. (A) 830 nm spectrometer design using a linescan CCD camera. (B) 1040 nm swept-source system using a balanced detection configuration. FBG: Fiber Bragg grating.

4. Results

Figure 3 shows a plot of maximum velocities obtained from a capillary tube containing 1% intralipid flowing at different speeds imaged using both the spectrometer-based and swept-source systems. All velocities reported here are the normalized maximum velocities as given

by Eq. (13). As predicted by Eq. (6), phase wrapping occurs at the same threshold velocity for each system when $V' = 1$.

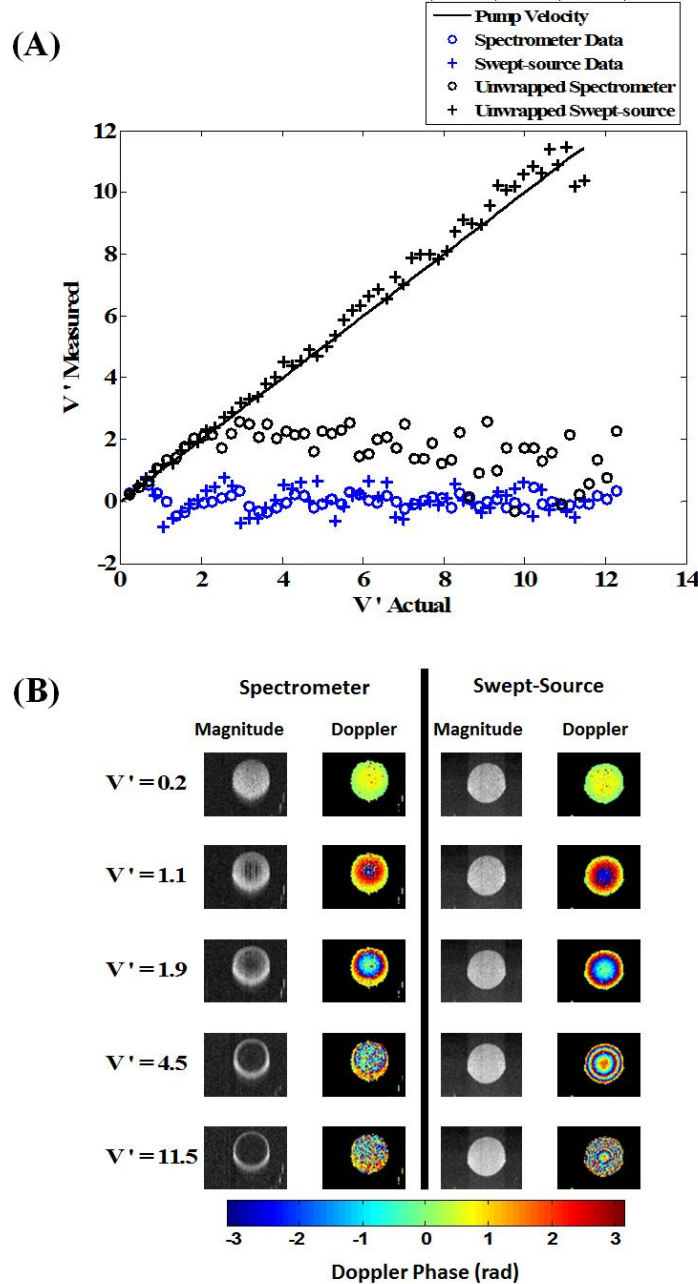


Fig. 3. Doppler phantom experiment results comparing flow velocity as measured using both systems described in Fig. 2. (A) Plot of measured velocities normalized to the theoretical wrapping velocity of each system. Blue coded data points show measured maximum velocities before phase unwrapping. Black coded data points show maximum velocities measured after phase unwrapping. (B) Cross-sectional magnitude and Doppler images with 100 kHz acquisition rates from both spectrometer-based and swept-source systems acquired at different flow velocities. The spectrometer-based system shows significant washout effects when $V' = 1$ while the swept-source data remains robust even at velocities 11 times the v_{wrap} limit.

As predicted by Eq. (11), the fringe washout effect is noticeable in the spectrometer-based system data when $V' > 1$. This effect results in a loss of signal in the center of the spectrometer-based magnitude images as shown in Fig. 3(B). Data acquired with the swept-source system showed constant magnitude images across all tested velocities and revealed multiply wrapped flow profiles.

Phase unwrapping was performed using a quality guided phase map [44]. Once unwrapped, the swept-source data showed good correlation with the expected center velocity predicted by parabolic laminar flow theory as shown in Fig. 3(A). After unwrapping, the spectrometer-based system showed comparable accuracy up to twice the washout limit. Beyond that velocity, significant SNR loss at the center of the capillary tube ultimately led to the complete loss of the Doppler signal at high velocities. The swept-source system demonstrated that the signal from the phantom remained strong even at high flow rates. Figure 3(B) shows examples of cross-sectional images from the flow phantom at the wrapping limit and at velocities high above the wrapping limit.

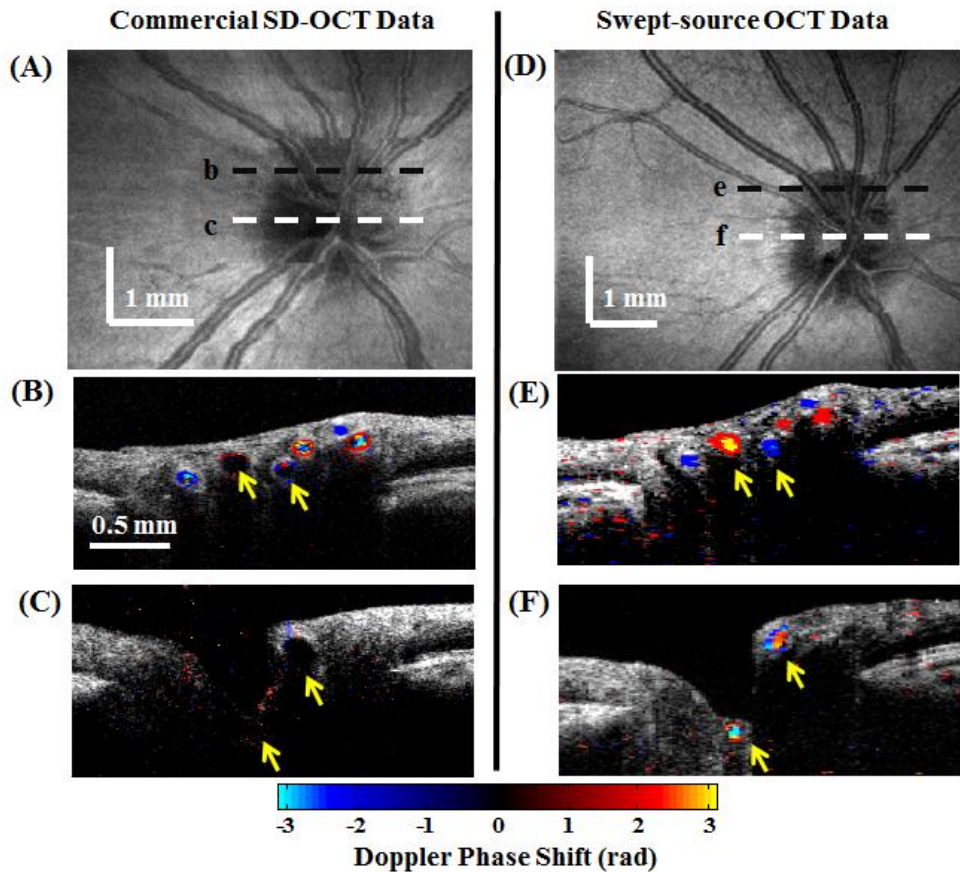


Fig. 4. Retinal data acquired from the optic nerve region of the left eye in the same subject using a commercial SDOCT system (A-C) and the custom swept-source system (D-F). (A) Retinal SVP image consisting of 512x200 lines from the SDOCT system. Dashed lines labeled *b* and *c* indicate positions of cross-sectional images in (B) and (C). (D) SVP image consisting of 256x200 lines from the swept-source system. Dashed lines labeled *e* and *f* indicate positions of cross-sectional images in (E) and (F). Yellow arrows indicate regions of washout caused by high blood flow. Fringe washout artifacts are present in the commercial SDOCT data. The swept-source data is free from washout artifacts allowing for flow detection in the indicated vessels.

Retinal data from a human subject was acquired using a commercial spectrometer-based OCT system operating at 20 kHz (Bioptrigen, Inc.). A volumetric data set of 512x200 A-scans was acquired over the optic nerve region of the retina to generate the summed volume projection (SVP) image shown in Fig. 4(A). Additionally, a Doppler volume of 512x50 A-scans with x6 oversampling in the fast scan dimension was acquired over the same area. Cross-sectional images with Doppler overlays are shown in Figs. 4(B) and (C). The indicated regions show large vessels with washout artifacts present in the optic disk. The swept-source system in Fig. 2 was adapted for retinal imaging. Volume data was acquired from the same eye of the subject at 256x200 lines with x6 oversampling in the B-scan dimension. The resulting SVP is shown in Fig. 4(D). Figures 4(E) and (F) show corresponding cross-sectional images to those in Figs. 4(B) and (C). A Doppler threshold of 0.3 radians was applied to data in Figs. 4(B) and 4(E) and 0.7 radians to data in Figs. 4(C) and 4(F) to adjust for uncorrected bulk motion artifacts. The washout artifacts were eliminated in the swept-source data, allowing for the detection of flow in the major vessels at the center of the nerve head as well as in the large branch vessels.

4. Discussion

Swept-source systems have a significant advantage over spectrometer-based systems in measuring high flow rates. Although it has been previously discussed that swept-source systems do not suffer the same fringe washout effects as in spectrometer-based systems, high velocities may still induce fringe washout with swept-source detection. Washout results when the phase shift over a single integration period for each wavelength channel is π . As described from Eq. (11), this limit scales with the number of spectral samples in swept-source detection schemes for a given sweep rate. The spectral sampling frequency plays a direct role in washout effects. If the interferometric fringe shifts caused by moving scatterers are not sampled at or above Nyquist, then a π Doppler shift results in SNR loss due to fringe averaging and signal aliasing. While it has been shown that qualitative flow imaging methods may detect regions of slow flow with more sensitivity than phase-based quantitative techniques [15], v_{wash} determines the maximum scatterer speed detectable for all flow imaging methods before severe signal loss occurs.

Axial motion of the sample during data acquisition in swept-source systems gives rise to an additional shift in the detected axial position of moving scatterers. Based on the axial velocities, v_z , used in the phantom experiments, the expected axial shift may be calculated using [28]

$$\delta z = \frac{k_o}{k_1} v_z, \quad (14)$$

where k_o is the center wavenumber of the swept-source and k_1 is the wavenumber linear tuning slope given as $k_1 = \Delta k / DT$, the sweep bandwidth divided by the time for the forward sweep of the laser. For the swept-source system used in Fig. 2, $k_o = 6.037 \times 10^3 \text{ mm}^{-1}$ and $k_1 = 1.167 \times 10^8 \text{ mm}^{-1}\text{s}^{-1}$. The fastest measured axial velocity for the phantom study was 246 mm/s, corresponding to an axial shift of 12.6 μm , or 2.3 axial pixels in a given SSOCT image. Thus, the effects of this artifact in the phantom studies is expected to be small compared to the 600 μm diameter of the capillary tube. However, correction for the shifting artifact is still desirable.

To correct for the axial shifting artifact in SSOCT, the shift of each pixel for a given A-scan was calculated from the observed axial velocity profile according to Eq. (14). This shift corresponds to the actual location of the observed velocity values for a given A-scan. A linear interpolation of the velocity value back to the observed location in depth was computed, thus creating a new, deshifted velocity profile. As a demonstration of this correction, Fig. 5 shows a B-scan frame of the fastest tested flow velocity from the phantom experiment. After velocity interpolation is performed, the corrected image is slightly shifted in depth, but the change is difficult to observe due to the small magnitude of the pixel shift. The velocity profiles in Fig.

5(C) show a slight shift due to the correction. The minute change in position demonstrates that axial shifting artifacts had little effect on the data presented here, even when measuring high flow rates.

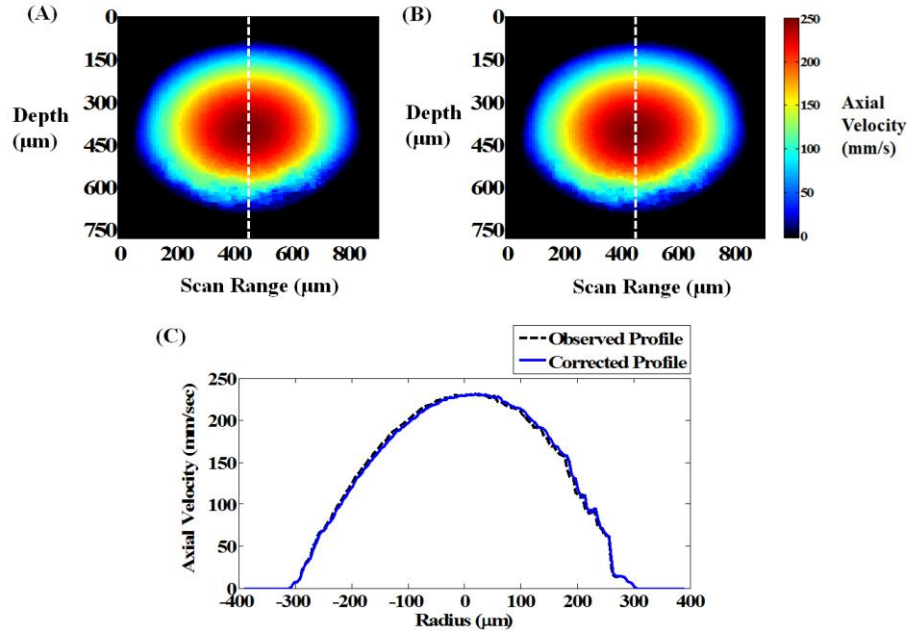


Fig. 5. Axial shift correction of SSOCT Doppler image by velocity interpolation. (A) Original Doppler B-scan image of the flow phantom at the highest tested speeds after phase unwrapping. (B) Corrected Doppler image using velocity interpolation. (C) Velocity profiles taken from (A) and (B) along the dashed line. The axial shift artifact does not contribute significantly to the image as seen by the close correlation of the original and corrected profiles.

Differences in the optical absorption and scattering of the intralipid at 830 nm and 1040 nm should also be considered. For intralipid, scattering is the dominant property and differs by approximately a factor of two between the two wavelengths ($\mu_s \sim 200 \text{ cm}^{-1}$ at 830 nm and $\mu_s \sim 100 \text{ cm}^{-1}$ at 1040 nm) [45]. Optical absorption properties at this wavelength also differ ($\mu_a = 0.02 \text{ cm}^{-1}$ at 830 nm and $\mu_a = 0.1 \text{ cm}^{-1}$ at 1040 nm) [46]. In blood vessels, differences in optical properties are also present ($\mu_s = 280 \text{ cm}^{-1}$, $\mu_{a-HbO} = 1.0 \text{ cm}^{-1}$, $\mu_{a-Hb} = 1.3 \text{ cm}^{-1}$ at 830 nm and $\mu_s = 200 \text{ cm}^{-1}$, $\mu_{a-HbO} = 0.8 \text{ cm}^{-1}$, $\mu_{a-Hb} = 1.3 \text{ cm}^{-1}$ at 1040 nm) [47]. While optical absorption is similar, optical scattering properties differ by ~20%. These differences in optical properties affect the signal level of the sample during OCT acquisition. However, as long as the signal is sufficiently high, the velocity measurements should be unaffected by these differences.

The spectrometer-based Doppler data shown in Fig. 3B shows a slight vertical offset of the maximum velocity in the B-scan images of the intralipid phantom flowing through the capillary tube. This is believed to be caused by bending in the tube connecting the syringe to the capillary tube. It is known that fluid flow through a curved pipe may cause slight offsets in the velocity distribution at locations upstream from the bend due to secondary flow effects and pressure gradients orthogonal to the direction of flow [48].

The spectrometer-based data acquired in Fig. 4 was acquired at a rate five times slower than the swept-source data. However, the images in Fig. 4(A-C) are clinically representative of standard commercial systems. Based on Eq. (6), v_{wrap} for the 100 kHz swept-source system was 19.2 mm/sec using $n = 1.38$ for blood and $\lambda_o = 1040 \text{ nm}$. For a spectrometer-based system at 100 kHz and $\lambda_o = 830 \text{ nm}$, $v_{wrap} = 15.0 \text{ mm/sec}$. Phase wrapping artifacts were still present in the swept-source data, and would similarly appear in spectrometer-based data acquired at

the same rate. However, even high speed spectrometer-based data would still suffer signal loss in the major vessels due to fringe washout.

For the spectrometer-based system, $v_{wash} = 23.9$ mm/sec, with $n = 1$ for on-axis sample motion. For the swept-source system, $v_{wash} = 7.2 \times 10^4$ mm/sec. In biological samples, the rate of fluid flow will typically be far below v_{wash} for swept-source systems. However, spectrometer-based systems may still suffer significant signal loss when imaging large vasculature with high flow velocities. Velocities in the major arteries near the optic nerve have been measured in the range of 30-100 mm/sec [26,49]. Imaging such speeds is problematic for current high speed spectrometer-based systems. Swept-source systems would not suffer signal degradation, though phase wrapping may still occur. Accurate flow profiles may be reconstructed with appropriate unwrapping methods. While swept-source systems possess an inherent advantage for imaging high flow rates, further development of fast cameras may allow spectrometer-based systems to reduce or avoid biological washout effects as well.

5. Conclusions

We have shown results comparing the advantages and limitations of swept-source versus spectrometer-based systems for Doppler flow imaging. The cause of phase wrapping is clearly distinguished from that of washout, the former being caused by phase changes between Doppler A-scans and the latter being caused by phase changes within the acquisition time of a single A-scan. Swept-source systems demonstrate potential for enhanced imaging of fast flows due to their robustness against fringe washout effects compared to spectrometer-based systems. Motion-induced signal loss is typically not noticeable in swept-source systems because the integration period for each spectral channel is much smaller than the integration and readout time of the entire A-scan spectrogram. This is an important consideration for clinical applications where major vessels with high flow rates are imaged. The ability to visualize and measure blood flow in the major arteries could be of significant help in the clinical analysis of total retinal flow.

Acknowledgments

The authors acknowledge financial support from NIH R01-EY-014743 and NIH R21 EB 006338. We also thank Ramiro Maldonado and Anthony Kuo for assistance with acquiring the commercial system retinal data and Sina Farsiu for fruitful discussions on the axial shifting correction.